Int. J. Heat Mass Transfer. Vol. 36, No. 4, pp. 1061–1072, 1993
Printed in Great Britain

0017–9310/93 $6.00 + 0.00

Structure of air–water bubbly flow in a vertical pipe—II. Void fraction, bubble velocity and bubble size distribution

T. J. LIU† and S. G. BANKOFF
Chemical Engineering Department, Northwestern University, Evanston, IL 60208-3120, U.S.A.

(*Received* 24 *June* 1991 *and in final form* 24 *January* 1992)

Abstract—In a companion paper (Liu and Bankoff, *Int. J. Heat Mass Transfer* **36**, 1049–1060 (1993)) measurements were presented of liquid-phase velocity and turbulence properties in air–water bubbly upflow under a range of flow conditions. In this paper measurements of the radial profiles of void fraction, bubble velocity and bubbly size, using a miniature dual-sensor resistivity probe, under the same conditions are presented. A new digital processing method, based on threshold combinations of level and slope, was developed for phase identification by the resistivity probe. Local mean bubble sizes ranged from 2 to 4 mm. The profiles of void fraction, bubble frequency and bubble size are found to show distinct peaks near the wall, becoming flat at the core. Experimental findings and parametric trends based on the effects of superficial velocities of both phases are summarized and discussed.

INTRODUCTION

TWO-PHASE upward cocurrent bubbly flow in a circular pipe may exhibit bubble layers near the wall (Serizawa *et al.* [1], Wang [2], Michiyoshi and Serizawa [3]), or bubble coring (Welle [4], Jones and Zuber [5], Herringe and Davis [6]), in which the maximum bubble concentration occurs at the center of the pipe, depending on the flowrates, but also on other flow conditions which are imperfectly understood. A previous paper (Liu and Bankoff [7]) presents systematic liquid-phase measurements for 48 combinations of gas and liquid flow rates. This is a companion paper, giving radial distribution measurements with a dual-sensor resistivity probe of the corresponding gas-phase local parameters, which are the void fraction, bubble frequency, bubble mean velocity, bubble velocity turbulent intensity and spectrum, and bubble size distribution. The experiments were conducted with six different superficial liquid velocities (J_f) from 0.376 to 1.391 m s^{-1}, with seven superficial air velocities (J_g) from 0.027 to 0.347 m s^{-1}. Thus, a total of 42 combinations of two-phase flow conditions were employed. The local void fractions ranged up to 50% and average void fractions up to 42%. A special bubble generator was designed to generate bubbles of 2–4 mm mean diameter, depending on the flow conditions, at the measuring station ($L/D = 36$). Some comparisons are made with existing data under similar conditions, and with empirical models. However, the principal value of the present work is to serve as a reliable and fairly complete data base for development of new physical models and for code validation.

A miniature dual-needle electrical resistivity probe was coupled with a driving circuit to measure the gas-phase local parameters. The sensing element was made from a 0.1 mm OD stainless steel drill, of which one side was ground to give a sharp penetrating tip. The other side of this small needle was inserted and welded into a 0.2 mm OD, 0.1 mm ID, stainless steel hypodermic tube, which was insulated by a hot shrinkable tube to serve as a signal conductor. The sensing needle was electrically insulated and made non-wetting by the application of varnish and a teflon coating, except at the very tip. Shadow micrographs of the tip indicated that the tip diameter was within 5 ~ 8 μm. This tip was able to pierce, with small deformation, fast-moving small bubbles at the point of impact, leading to a fast signal response. Two separate identical sensors were encased in a 30 mm long, 3 mm OD stainless steel tube to form a dual-sensor resistivity probe for bubble velocity measurements. The outer stainless steel sheath provided a well-defined distance between tips, as well as a common ground. An axial distance of 5 mm between two needle tips was selected to measure bubble velocity with sufficient accuracy. Details of the design of the probe are given in Liu [8].

Each sensor was driven by a voltage-sensitive circuit consisting of a 1.5 volt battery and a 100 kΩ potentiometer connected in series with the probe to ground. The instantaneous changes of local resistivity in the two-phase stream were detected by a voltage signal between the needle tip and the ground. The voltage drop across the probe during closed circuit (liquid signal) approximated 0.3 ~ 0.4 volts. This low voltage effectively reduced electrochemical phenomena at the

† Present address: Institute for Nuclear Energy Research, P.O. Box 3-3 Lung Tan, Taiwan 32500, Republic of China.

NOMENCLATURE

d	axial distance between the tips of resistivity probe
D	diameter of pipe
D_{av}	local mean bubble diameter
F_{ab}	cross-correlation function of a and b
J_f, J_g	superficial velocity of liquid and gas flow
L	entrance length
r	coordinate in radial direction; $r = 0$ at pipe center
R	Radius of pipe
u_b	root-mean-square value of instantaneous local bubble velocity fluctuation
U_b	local bubble velocity
U_f	local liquid phase velocity
x	bubble chord length
$\langle\ \rangle$	averaged over cross-sectional area
$\langle\alpha\rangle$	mean void fraction measured by hold-up method.

Greek symbols

α	local void fraction
$\bar{\alpha}$	mean void fraction integrated by local value.

sensor. In order to keep the phase variation signal clearly defined, after each run (approx. one hour), the probe tips were carefully cleaned. The analog output signals of the two sensors were sampled by a model TSI IFA-200 multichannel digitizer. Zero time shift between these two signals was checked in advance to ensure the accuracy of bubble velocity measurements. A typical signal at the air–water interface is shown in Fig. 1. Following digitization, status data were sent to the computer and stored for later analysis. A sampling rate of 10 kHz per channel was used to ensure sufficient resolution in analyzing the high-speed, small bubble, two-phase conditions. A sampling time of 10 s proved satisfactory for statistical analysis with detection of a sufficient number of bubbles for most of the flow conditions. For high liquid flow and low gas flow conditions, a sampling time of 30 s was used. The measurements of the corresponding liquid-phase local parameters, using well calibrated one- and two-dimensional hot-film anemometers, under the same flow conditions and test matrix have been given elsewhere [7, 8].

PHASE DISCRIMINATION AND DATA PROCESSING

Many investigators, including Serizawa *et al.* [2], Herringe and Davis [6, 9], and Uga [10], have used a Schmitt trigger circuit to transfer an original analog signal to a binary data series by presetting the trigger level, and then processed these binary data statistically. Each investigator used a different method for the trigger level setting. However, the accuracy of this level setting directly affects the accuracy of void fraction, bubble velocity and bubble size measurements, owing to the finite rise and fall time of bubble–probe interaction. Theoretically, this trigger level should be set as close to the liquid level as possible. However, the liquid-level signal depends on the test flow conditions, water conductivity, drift due to tip fouling, bubble–probe interaction and the wettability of the sensing surface. From the signal on the oscilloscope and digitized raw data, one could observe that even the minimum value may not be the pure liquid signal, due to overshooting. It was found that even for a single radial point measurement, it was difficult to set the signal trigger level effectively to solve this phase discrimination problem.

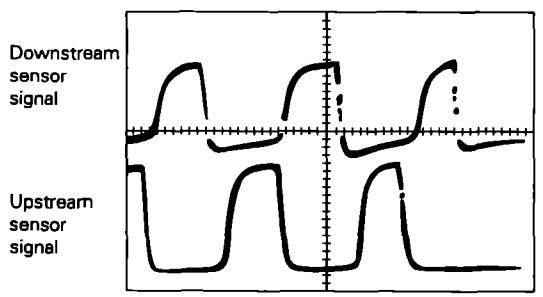

Fig. 1. Typical resistivity probe response in two-phase bubbly flow.

In this study, an iterative routine of self-adjusted level and slope phase discrimination scheme for each sub-block (about 2000 samples) of raw data was developed, based on the assumption that the trigger level was independent of radial position. Before a data sub-block entered the phase discrimination routine, the maximum (M) and minimum (N) values of signal were determined in advance. Let the initial level (T) and slope (S) threshold be

$$T = (M-N)\cdot C+N \qquad S = (M-N)\cdot E$$

where C and E are the initial preset values. Let R_i be the ith sampled datum in millivolts and define

$$P_f = R_{i-1} - R_i \text{ (Forward slope)}$$

$$P_b = R_{i+1} - R_i \text{ (Backward slope)}$$

$$R_f = |P_f|, \qquad R_b = |P_b| \text{ (Magnitude of } P_f \text{ and } P_b).$$

If any one of the following four conditions is valid, then R_i is in liquid phase; otherwise, it is in gas phase.

(1) R_{i-1} in liquid $R_i > T$ $R_f < S$ $0 < P_b < S$

(2) $R_i > T \quad R_{i+1} < T \quad 0 < P_f < S \quad R_b < S$

(3) $R_i < T \quad R_f < S \quad R_b < S$

(4) $R_{i+1} > T \quad R_{i-1} > T \quad P_f > K \quad P_b > K$.

Condition (4) is used to check for closely-packed bubbles. As shown in Fig. 1, due to a very sharp voltage signal increase and decrease when a bubble hits and leaves the probe tip, at the 10 kHz sampling rate, E was set to $C/3$ and $K = C/9$ was satisfied in all test conditions. Therefore the only variable that should be adjusted is C. A trial value of C was used for the data blocks at each local measuring point for the phase discrimination and labelling. As expected, most of the liquid phase data fell into condition (3). Then the area-average void fraction, $\bar{\alpha}$, from integrated local void fraction measurements, was compared with average void fraction $\langle\alpha\rangle$ from hold-up measurements. The reproducibility of the hold-up measurements was within 0.5% for most of the flow conditions. If the ratio of $\bar{\alpha}/\langle\alpha\rangle$ lay within the acceptable range of 0.96–1.03, the local void fraction was adjusted to satisfy $\bar{\alpha} = \langle\alpha\rangle$, and further statistical analysis began. Otherwise, a routine was actuated to adjust the value of C and iteration was continued. The new value of C depends on how closely the two void fractions ($\langle\alpha\rangle, \alpha$) agreed. Generally, a value of C within 0.2–0.3 would converge to the acceptable range. The good performance of this combined level (T) and slope (S, P_f, P_b, R_f, R_b) threshold algorithm for phase identification was confirmed by carefully checking all the labelled sampling data at each radial position.

The main advantage of the iterative scheme accompanying this phase discrimination method is that every sub-block has a flexible trigger level, even for the same value of C. This is of practical significance if the output of two sensors is in different voltage levels or sensor drifts. The smaller number of samples in each sub-block ensures the elimination of the error due to such phenomena as flow condition, radial position, probe drift, etc. In addition, the integrated void fraction automatically converges to the measured mean $\langle\alpha\rangle$ to ensure the accuracy of local void fraction results. This resistivity probe data processing method can be further applied to other flow conditions and flow regimes to analyze the dispersed phase signals.

LOCAL PARAMETERS ANALYSIS METHODOLOGY

Void fraction and bubble frequency

Based on the aforementioned phase discrimination scheme, the probe analog signal is converted into a binary signal $\delta(r, t)$, which equals one in the gas phase and zero in the liquid phase. The local void fraction in a quasi-steady two-phase flow, as measured by the upstream sensor of the dual-sensor resistivity probe, is determined by the time average of $\delta(r, t)$. To digitize the signal, with total sample number N, the local void fraction can be expressed as

$$\alpha(r) = \frac{1}{N}\sum_{i=1}^{N}\delta(r, t_i). \tag{1}$$

The local bubble frequency, defined as the number of bubbles that pass through the point per unit time, averaged over a suitably long time interval, can also be measured by the upstream sensor of the resistivity probe.

Bubble velocity and its spectrum

Ideally, all the bubbles are in uni-directional motion, and a bubble hitting the first sensor will subsequently hit the axial downstream second sensor. The time-averaged local bubble velocity U_b can be determined if the bubble mean transport time, τ_0, and the axial distance between the tips of the sensors, d, are known. Thus

$$U_b = d/\tau_0. \tag{2}$$

In this study, both a multichannel analysis and a cross-correlation method were used to determine τ_0. The former method gives the spectrum of the time lag for each bubble, while the latter gives the most probable time lag between the two sensor output signals. For multichannel analysis, a computer subroutine was developed to transfer the transport time τ_i of each bubble to an amplitude pulse, and to count these pulse trains in 400 equally-spaced channels between the detected maximum and minimum of the pulse to yield the bubble velocity spectrum. Unfortunately, miscounting was inevitable in the actual measurement. This happens if a bubble is only pierced by one of the needles, or if before a bubble penetrates the first sensor, another bubble hits the second sensor. Then, the time lags for individual bubble transport may cause the apparent bubble transport time to be negative, which is physically impossible.

This miscounting problem was solved by eliminating the miscounted bubbles through a subroutine to identify the probe signals originating from the same bubble. Prior to identifying the miscounted bubbles, the beginning and end of the time address for individual bubbles were obtained. Then a multichannel analysis was performed to get the bubble velocity spectrum. Generally, 10–15% of the total number of bubbles were miscounted. The local bubble velocity $U_b(r)$ and its turbulent fluctuation $u_b(r)$ were determined by

$$U_b(r) = \sum_i N_i U_{bi}(r) \Big/ \sum_i N_i \tag{3}$$

$$u_b(r) = \left\{\sum_i N_i [U_{bi}(r) - U_b(r)]^2 \Big/ \sum_i N_i\right\}^{1/2} \tag{4}$$

where U_{bi} is the instantaneous measured local bubble velocity in the ith channel, and N_i is the counting rate of U_{bi} in each channel. In order to verify the validity

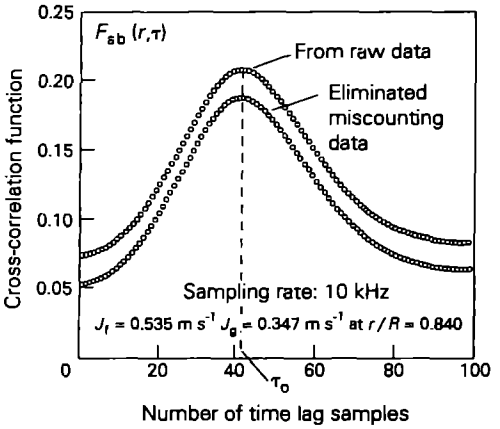

FIG. 2. Typical correlogram of two-needle resistivity probe output signals.

of the above method, the two tensor output signals a and b were checked by calculating the cross-correlation function F_{ab}, which is defined as

$$F_{ab}(r,\tau) = \lim_{T\to\infty} \frac{1}{T}\int_0^T a(r,0,t)b(r,d,t+\tau)\,dt. \quad (5)$$

All the correlograms obtained from the dual-sensor resistivity probe displayed a fairly distinct peak at each local point across the section. A typical correlogram is shown in Fig. 2. The most probable transport time (τ_0) at the clearly-defined peak of the function is used to determine the local mean bubble velocity $U_b(r)$. In the data processing, the cross-correlation function of the raw sampled data and the data eliminated due to miscounting were calculated in each local point. It is interesting to find that both sets of input data give the same values of the most probable bubble transport time, and hence the same bubble velocities. It would be expected that the small number of miscounted bubbles would not affect the position of maximum cross-correlation, except that the magnitude of the correlation coefficients would decrease. This feature improves the reliability of the bubble velocity results.

The bubble velocity obtained by the multichannel method was very close to the one obtained from the cross-correlation method in the core region ($r/R \leqslant 0.8$), with an average $\pm 2\%$ deviation. However, in the wall region ($r/R > 0.8$) the velocity was 2–4% higher for the multichannel method. In the present study, most of the bubble velocity data in the core region ($r/R \leqslant 0.8$) resulted from the cross-correlation method, which needed only a relatively small number of bubbles to get an accurate result.

Bubble chord length and size distribution

Even though the local void fraction distribution offers valuable information, it does not completely reflect the internal structure of the two-phase system. The same void fraction may be due to either a large number of small bubbles or a small number of large bubbles. Since the two cases differ both in average bubble size and in interfacial contact area, it was considered essential to complement the void fraction by a suitable measurement of average bubble size distribution.

The local bubble size can be determined from the measured bubble chord length spectrum based on a statistical treatment of the bubble residence time. For a fixed sampling rate, SR, and N_i samples counted in the ith bubble, the bubble chord length can be determined from

$$x_i = (N_i/SR)\cdot U_b. \quad (6)$$

However, a certain chord length may correspond to a small chord length in a large bubble or a large chord length in a small bubble, depending on the bubble–sensor interaction, bubble velocity, bubble shape and trajectory. The transformation of the measured chord length into a bubble diameter is still a difficult problem. In general, the bubble size distribution is related to the probability density function (pdf) of bubble chord length. Limited studies have been done on this problem. Bankoff [11] and Anderson [12] were the first to derive an integral equation which related bubble size pdf to the bubble residence time pdf under the assumptions of (i) spherical bubble and (ii) uni-directional bubble velocity that would not slow down and not be deflected by the probe, so that any element of the projected bubble frontal area would have equal probability of being detected.

Uga [10] and Herringe and Davis [9] derived a differential equation which related the bubble diameter pdf, $F(x)$, to the measured chord length pdf, $g(x)$, as

$$F(x) = 1/2[g(x) - x\cdot g'(x)] \quad (7)$$

based on the same assumptions. Using equation (7) to obtain the distribution $F(x)$ requires differentiation of the measured irregular curve of $g(x)$, and this operation will magnify any scatter to induce uncertainty. However, the local average bubble diameter, $D_{av}(r)$, can be determined by integration of measured bubble chord length pdf as:

$$D_{av}(r) = \lim_{D\to\infty}\int_0^D DF(D)\,dD = 1.5\int_0^\infty xg(x)\,dx. \quad (8)$$

Recently, Clark and Turton [13], with the assumption (ii) above for some well-defined bubble shapes, provided information about the transformation between bubble size and chord length pdf. However, it is hard to use a more sophisticated bubble shape in this analysis, owing to the lack of detailed knowledge on the bubble shape in two-phase turbulent flow. In practice, the presence of the irregular bubble chord length pdf also made it difficult to transform. Serizawa *et al.* [14] recently derived an integral equation, similar to the Bankoff approach, to calculate spherical bubble size distribution from the bubble chord length pdf,

which takes into account the effect of multi-directional bubble movement. However, this requires three-dimensional bubble-velocity measurements, which are scarce or non-existent. Therefore, only results of chord length distribution, instead of bubble size distribution, were demonstrated.

The method of Uga [10] and of Herringe and Davis [9] was used to interpret our data in terms of bubble size. It was reasonable to assume that the small bubbles (2 ~ 4 mm dia.) were nearly spherical (Matsui [15]). The second assumption of unidirectionality was generally true when the measuring point was far from the wall (relative to bubble size), using a very small sensing tip (5 ~ 8 μm dia.) in comparison with the detected bubble. At every local measuring point, 100 equally-spaced increments were divided between the measured maximum and minimum contact time. The bubble chord length pdf was then determined by multichannel analysis. Finally, the time averaged local bubble size was evaluated by equation (8). The accuracy of the measured bubble size was confirmed by pictures taken in the water-filled, transparent rectangular view box.

EXPERIMENTAL RESULTS AND DISCUSSION

Local void fraction and bubble frequency

Typical results for the void fraction and bubble frequency radial profiles are presented here in Figs. 3 and 4. Complete results [8] can be obtained from the authors. The bubbles tend to migrate toward the wall. Thus, the void fraction, as well as the bubble frequency profiles, under all the present test conditions, showed a distinct peak near the wall, and a relatively flat pattern in the core ($r/R \leqslant 0.8$).

A bubble in an inviscid shear flow experiences a Bernoulli lift force towards the center of the pipe. Very close to the wall, viscous effects are important, resulting in increased drag on the side of the bubble near the wall. This causes the bubble to rotate and roll along the wall, causing the stagnation point to be shifted away from the wall. Another possibility is that the bubble makes actual contact with the wall for some part of its residence time in the vicinity of the wall, and that surface tension forces then hold it against the wall. The theory for these effects has not yet been worked out.

As expected, increasing the gas flow rate at constant liquid flow rate increased the void fraction and bubble frequency, both in the core region, and in their peaking region near the wall. The axisymmetric void profiles confirmed that a fully-developed turbulent two-phase bubbly flow field had been closely approached. Wall peaking became more pronounced for high liquid flows, with a relatively sharp peak near the wall, and a small amount of bubbles nearly uniformly-distributed in the core region. However, at lower liquid flow rates, a more uniform void distribution with a relatively lower peak near the wall was observed at all gas flows. This difference in void distribution may be due to the balance between the buoyancy and inertial force in the axial direction, as well as the lateral lift force interaction with the bubble, dragging the bubble toward the wall.

The effect of increasing liquid flow at constant gas flow was to decrease the void fraction in the core region, as well as the void fraction at the peak near the wall. This tendency was somewhat related to the total gas volume flow rate under different flow conditions. At constant J_g, increasing J_f lowered the area-averaged void fraction $\langle\alpha\rangle$. The bubble frequency also decreases in the core region, but increases near the wall. This bubble redistribution is closely related to the local void fraction and bubble size. Since the increased segregation of bubbles near the wall at higher liquid flow conditions was not accompanied by a similar change in the bubble size distribution (Fig. 10), it follows that the bubble frequency near the pipe wall becomes larger for higher liquid flows.

Bubble velocity and its spectrum

Typical spectra obtained at various local positions are presented in Fig. 5. The detected spectrum at every local point covered a broad range of bubble velocities, approximately following a Poisson distribution. As shown in Fig. 6, increasing either gas flow or liquid flow increases the bubble velocity. There were no peaks in the bubble velocity profiles similar to those observed in wall peaking void profiles.

In order to check the accuracy of local measurements, the integrated local bubble velocity (U_b) was compared with the superficial gas velocity (J_g), which was directly measured from calibrated orifice flow meters. From the locally-measured α and U_b, we can calculate the area-averaged volume flow defined by

$$\langle\overline{J_g}\rangle = \frac{1}{A}\int_A (\alpha \cdot U_b)\, dA. \tag{9}$$

A total of 42 flow conditions were checked. As shown in Fig. 7, most of the individual data sets were within $\pm 5\%$. The reproducibilities of the local bubble velocity and the void fraction measured by resistivity probe were within 2%.

For upflow, the bubbles normally moved faster than the surrounding liquid due to buoyancy. The slip ratio between the phases was found to increase slowly in the core region, and increase sharply when close to the wall. As shown in Fig. 8, increasing the void fraction lowers the slip ratio.

Bubble velocity turbulence profiles

The bubble velocity turbulent fluctuation, as presented in Fig. 9, showed a fairly uniform radial distribution, except for the wall region. As expected, the effect of increasing gas velocity was to increase the bubble turbulence, owing to the increased bubble–bubble and bubble–liquid interactions. However, increasing the water flow at constant gas flow rate decreased the bubble turbulence at low flow con-

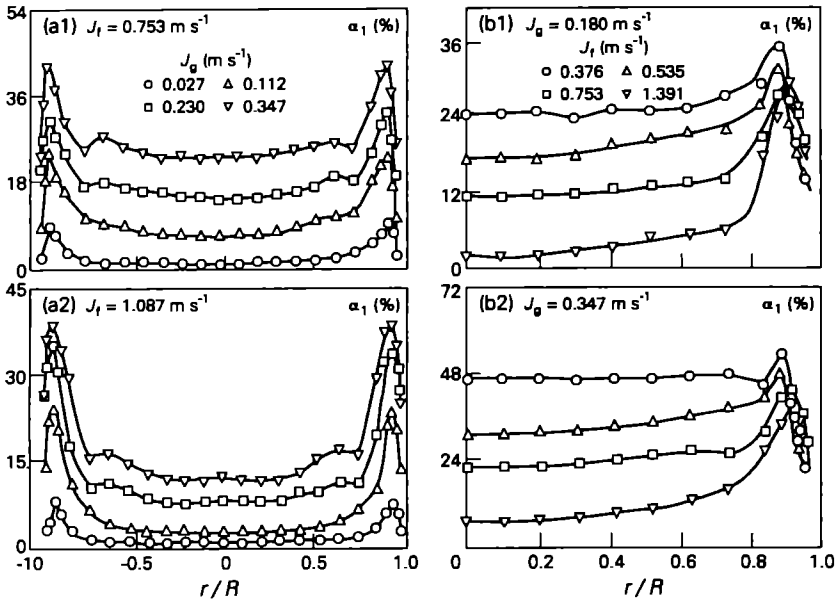

FIG. 3. Void fraction distributions (a) at constant J_f, (b) at constant J_g.

ditions (such as at $J_f = 0.376$, 0.535, and 0.753 m s^{-1}). On further increasing the liquid flow, a slightly-increasing effect was found, especially close to the wall. This phenomenon was observed at all gas flow conditions. This illustrates that the bubble–liquid interactions can be less efficient in producing turbulent energy in some velocity ranges than in others, possibly due to the damping effect of the water inertia. However, up to some higher flow limit, the absolute value of the bubble fluctuation always increased. In view of the decrease in mean void fraction in the latter case as the liquid flow rate is increased, it is found that the decrease in void fraction outweighs the contribution of increased single-phase turbulence as J_f increases at constant J_g. This somewhat surprising result illustrates the dominant effect of bubble–liquid interactions in producing liquid-phase turbulence under some conditions. This implies that the energy of the bubble shape oscillations becomes significant above some critical Reynolds number based on relative bubble velocity.

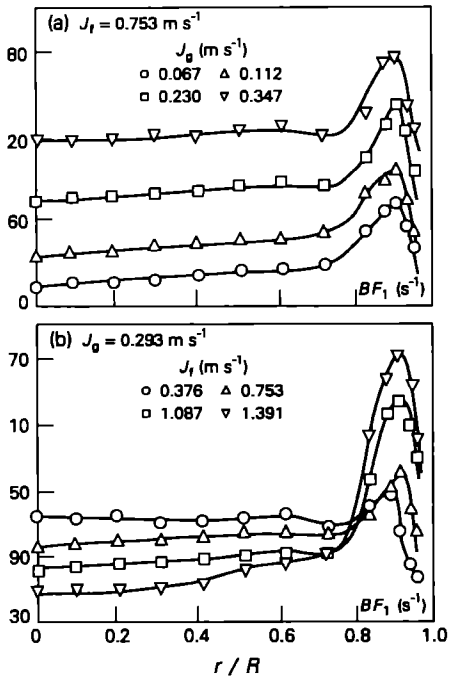

FIG. 4. Bubble frequency distributions (a) at constant J_f, (b) at constant J_g.

In order to make this effect clear, the relative bubble fluctuation (u_b/U_b) data are plotted in Fig. 10. The effect of increasing gas flow to u_b/U_b generally showed the same parametric trend as u_b in increasing the relative turbulence. However, the effect of increasing the liquid flow rate consistently resulted in decreased bubble relative turbulence. It is interesting to note that the bubble relative turbulent fluctuations at higher flow conditions (from $J_f = 0.753$–1.391 m s^{-1}) were almost merged together, but a distinct difference was found between the lower flow conditions. These results strongly imply that the local bubble turbulence is directly related to the local mean bubble motion.

Bubble chord length and size distribution

Typical bubble chord length spectra are presented in Fig. 11. The irregular distribution made it difficult to obtain bubble size pdf directly from equation (7) by differentiating the measured chord length pdf. Therefore, the local mean bubble diameter was obtained

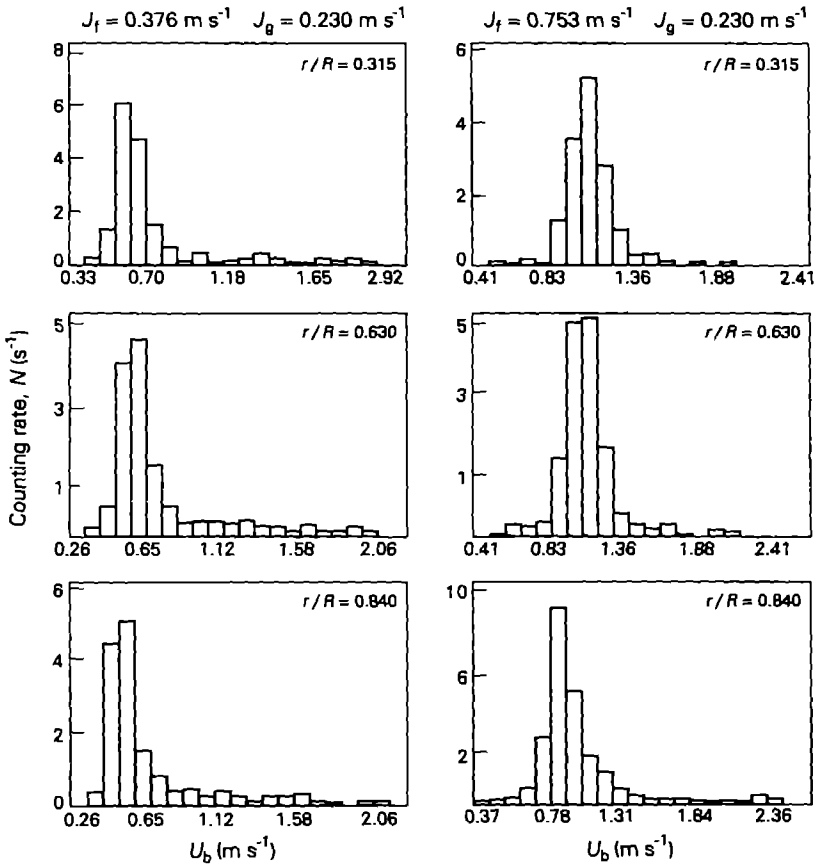

FIG. 5. Typical bubble velocity spectrum.

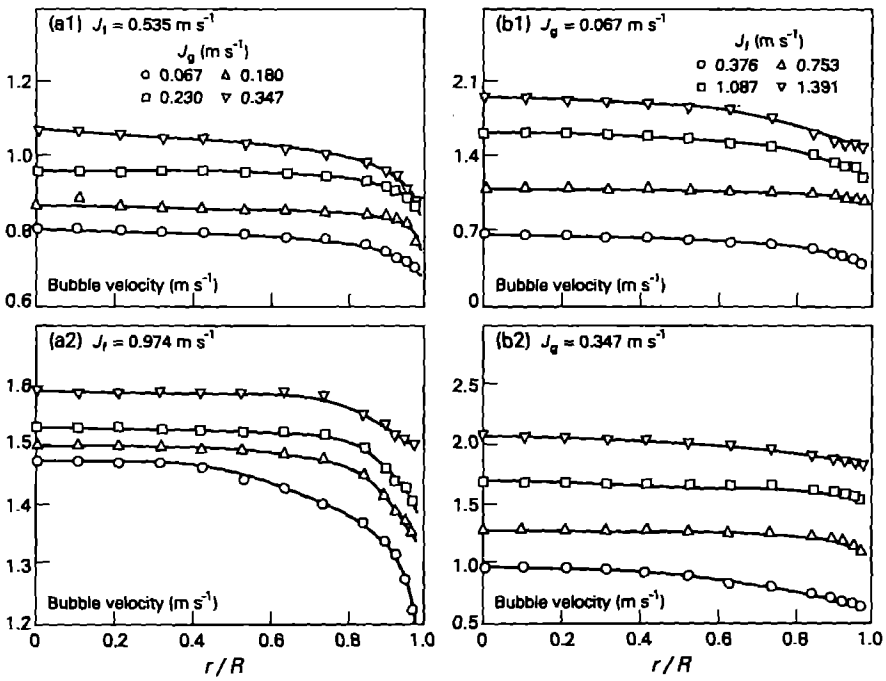

FIG. 6. Bubble velocity distributions (a) at constant J_f, (b) at constant J_g.

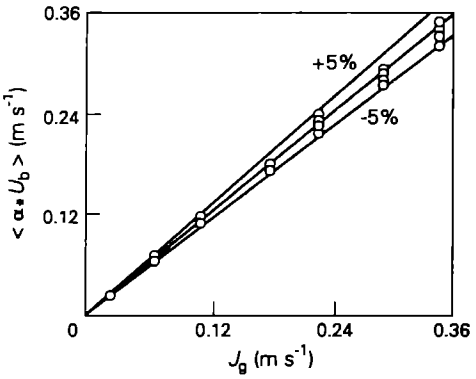

FIG. 7. Uncertainty estimation.

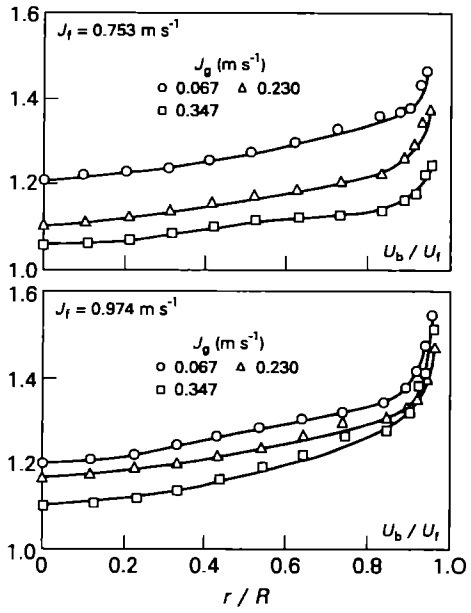

FIG. 8. Slip ratio distributions at various gas flows.

from an integration of the chord length pdf by equation (8). The detected local mean bubble sizes ranged from 2–4 mm in diameter depending on the flow condition and local position. The radial variations of mean bubble diameter are presented in Fig. 12. The accuracy of the measured bubble size was confirmed by the pictures taken in the view box. Typical results are shown in Fig. 13.

Generally, the mean bubble size profiles were fairly uniform over most of the pipe cross-section, except near the wall. The maxima were observed near the wall, at almost the same (or slightly closer) position as the void peaking. The same tendency was also reported by Michiyoshi and Serizawa [3] and Matsui [15]. The observed maxima near the wall may be explained in several ways. One reason may be that the highly concentrated bubbles had a higher probability to accelerate in the wakes of the other bubbles, finally coalescing with the other bubbles to form a larger bubble. A second reason may be the bubble elongation in the flow direction caused by the large gradient of the shear stress distribution close to the void peaking.

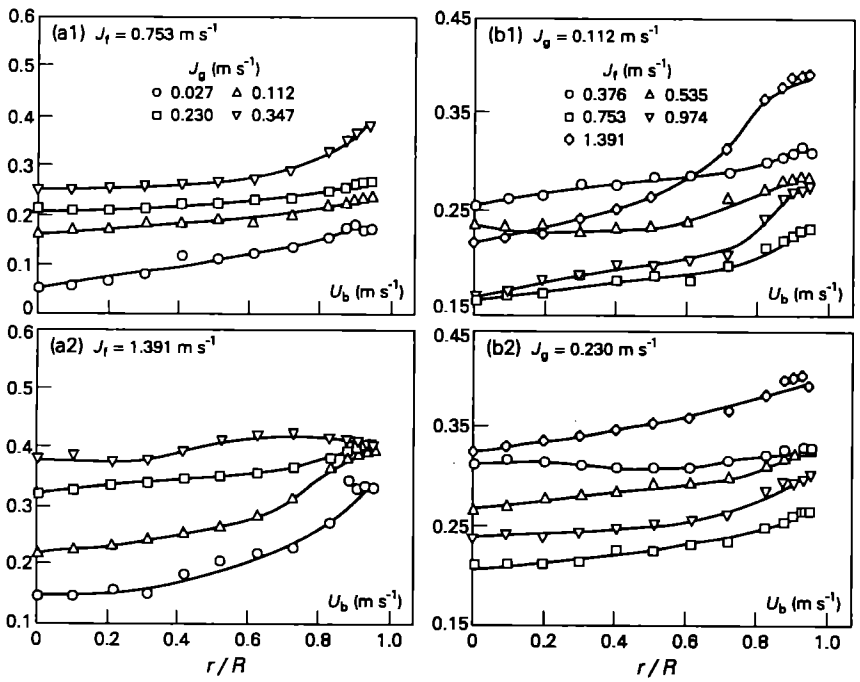

FIG. 9. Bubble velocity turbulent fluctuation (a) at constant J_f, (b) at constant J_g.

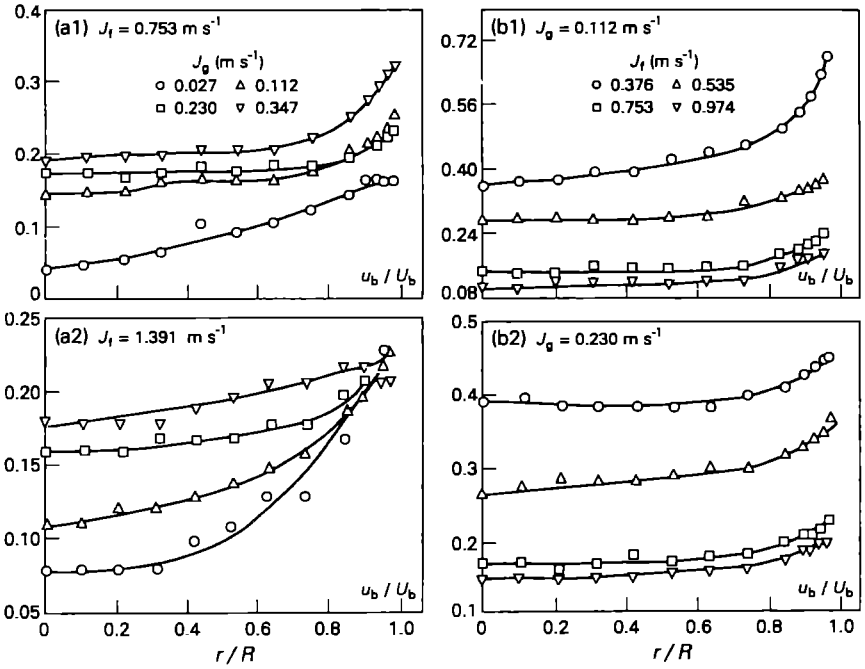

FIG. 10. Bubble relative turbulent fluctuation (a) at constant J_f, (b) at constant J_g.

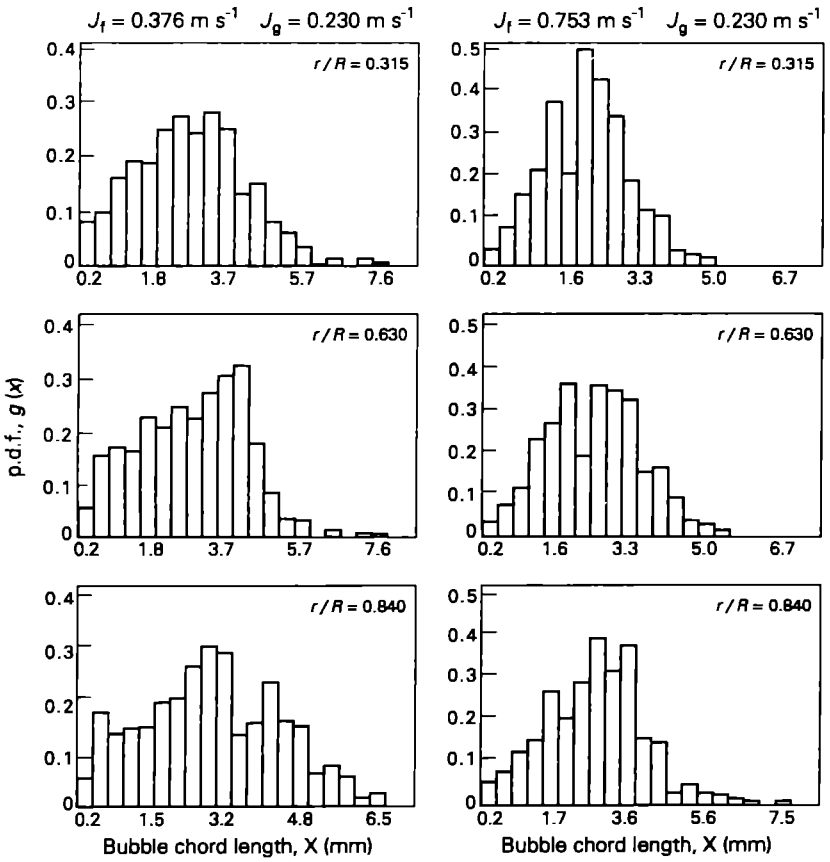

FIG. 11. Typical bubble chord length spectrum.

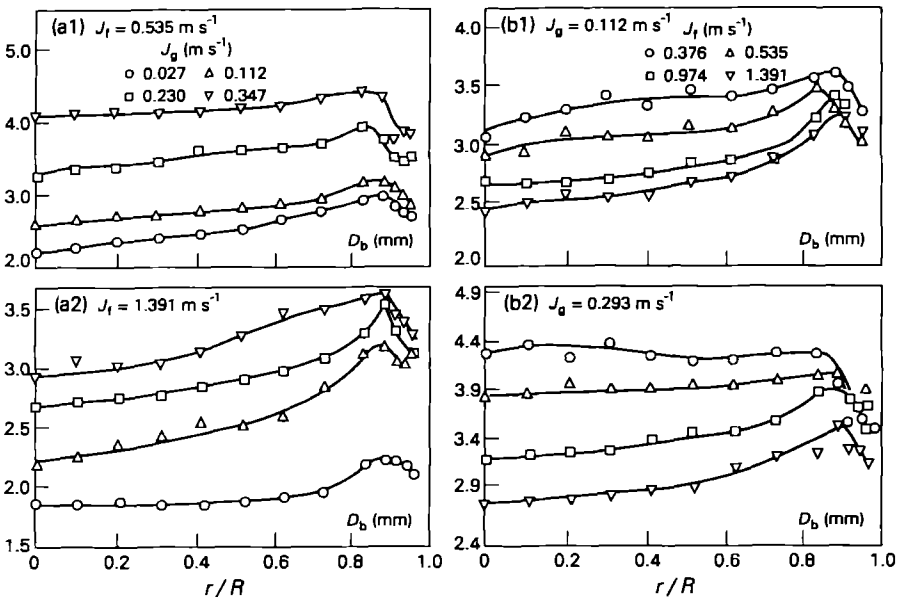

FIG. 12. Average bubble size distribution (a) at constant J_f, (b) at constant J_g.

Increasing the void fraction at constant water flow rate generally increased the bubble size, especially at low water flow conditions (Fig. 10). This may be the result of increased coalescence and also increased bubble detachment sizes. Conversely, increasing the water flow rate at a constant gas flow rate decreased the bubble size, because of decreased coalescence rates and smaller bubble detachment sizes from the hypodermic needles. Most of these smaller bubbles slide close to the wall and add a relatively small amount to the bubble flow in the core region. This bubble size effect on bubble movement was observed by Sekoguchi *et al.* [16] with a single bubble stream. The strong dependence of phase distribution and bubble

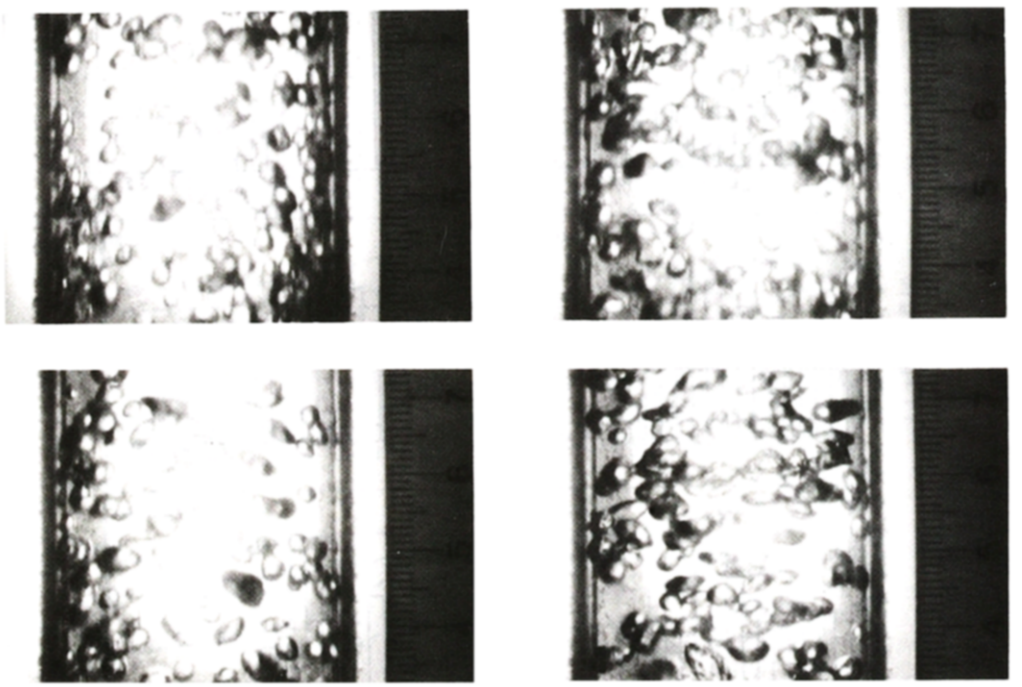

(a) [J_f = 0.535 m/s, J_g = 0.067 m/s] (b) [J_f = 0.535 m/s, J_g = 0.112 m/s]

FIG. 13. Typical bubbly flow photograph.

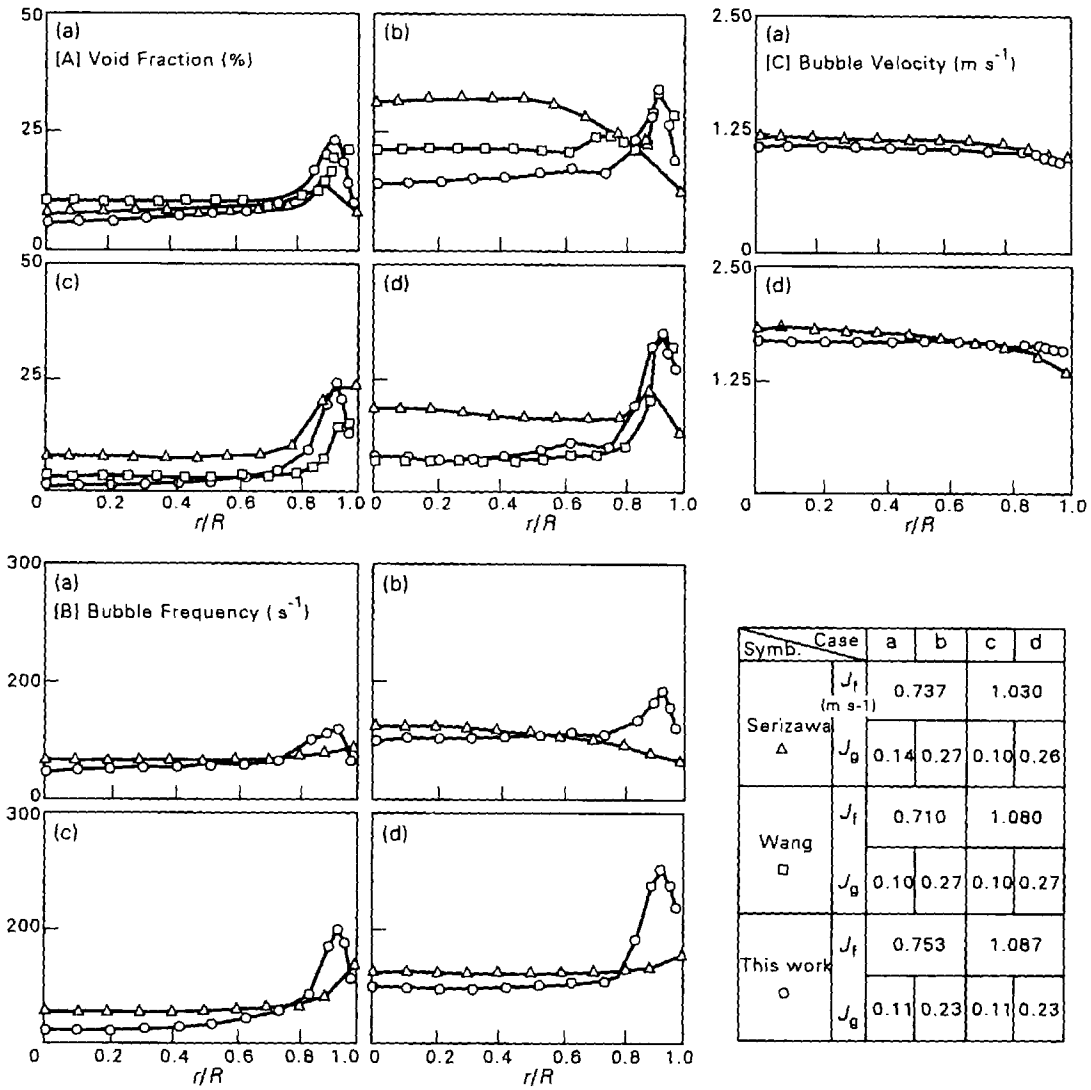

Symb. \ Case		a	b	c	d
Serizawa △	J_f (m s-1)	0.737		1.030	
	J_g	0.14	0.27	0.10	0.26
Wang □	J_f	0.710		1.080	
	J_g	0.10	0.27	0.10	0.27
This work ○	J_f	0.753		1.087	
	J_g	0.11	0.23	0.11	0.23

FIG. 14.

number frequency on bubble size distribution in a concentrated bubbly flow regime also was found in this study.

Data comparison

The present data of void fraction were compared with the data of Serizawa *et al.* [17] and Wang [4] under similar flow conditions. The bubble frequency and bubble velocity were also compared with the Serizawa *et al.* data. The results are shown in Fig. 14. It can be seen that large discrepancies exist. As discussed by these authors, the reasons may be due to the different entrance geometry and gas injection method, causing different size and configuration of bubbles. In fact, the different bubble size distributions may affect the local flow turbulent structure and also may even result in different flow regimes at the same liquid and gas flow conditions. Recently, experimental and theoretical studies on the interfacial area concentration in gas–liquid two-phase flow were carried out by Kataoka and Serizawa [18]. They concluded that the radial distributions of the interfacial area concentration were strongly affected by bubble size at the inlet which is controlled by the bubble generator. However, apart from the present study, no systematic and reliable experimental results on bubble size distribution have been obtained previously, making comparisons difficult under nominally similar conditions.

Acknowledgements—This work was supported by a grant from the National Science Foundation. Also, T. J. Liu was supported in part by the government of the Republic of China.

REFERENCES

1. A. Serizawa, I. Kataoka and I. Michiyoshi, Turbulence structure of air water bubbly flow, *Int. J. Multiphase Flow* **1**, 221–246 (1975).
2. S. K. Wang, 3-D turbulence structure measurements in air/water two-phase flows, Ph.D. Thesis, Rensselaer Polytechnic Institute (1986).

3. I. Michiyoshi and A. Serizawa, Turbulence in two-phase bubbly flow, *Nucl. Engng Design* **95,** 253–267 (1986).
4. R. V. Welle, Void fraction bubble velocity and bubble size in two-phase flow, *Int. J. Multiphase Flow* **11,** 317–345 (1985).
5. O. C. Jones, Jr. and N. Zuber, Use of a cylindrical hot-film anemometer for measurement of two-phase void and volume flux profiles in a narrow rectangular channel, in *AIChE Symp. Series: Heat Transfer—Research and Application* **74,** 191–204 (1978).
6. R. A. Herringe and M. R. Davis, Structure development of gas–liquid mixture flows, *J. Fluid Mech.* **73,** 97–123 (1976).
7. T. J. Liu and S. G. Bankoff, Structure of air–water bubbly flow in a vertical pipe: I. Liquid mean velocity and turbulence measurements, *Int. J. Heat Mass Transfer* **36,** 1049–1060 (1993).
8. T. J. Liu, Experimental investigation of turbulence structure in two-phase bubbly flow, Ph.D. Thesis, Northwestern University (1989).
9. R. A. Herringe and M. R. Davis, Detection of instantaneous phase change in gas–liquid mixtures, *J. Phys. E.: Sci. Instrum.* **7,** 807–812 (1974).
10. T. Uga, Determination of bubble-size distribution in a BWR, *Nucl. Engng Design* **22,** 252–261 (1972).
11. S. G. Bankoff, Bubble radius distribution functions from resistivity probe measurements, *A.I.Ch.E. Jl* **10,** 776 (1964).
12. T. T. Anderson, Comments on two-phase measurements using a resistive probe, *A.I.Ch.E. Jl* **10,** 776, 791 (1964).
13. N. N. Clark and R. Turton, Chord length distribution related to bubble size distributions in multiphase flows, *Int. J. Multiphase Flow* **14,** 413–424 (1988).
14. A. Serizawa, I. Kataoka, I. Zun and I. Michiyoshi, Bubble size effect on phase distribution, *Proc. Japan–U.S. Seminar on Two-Phase Flow Dynamics*, Ohtsu, Japan (1988).
15. G. Matsui, Characteristic structure of upward bubble flow under the same flow rate conditions, in *Proc. Japan–U.S. Seminar on Two-Phase Flow Dynamics*, Ohtsu, Japan (1988).
16. K. Sekoguchi, H. Fukui and Y. Sato, Flow characteristic and heat transfer in vertical bubble flow, in *Proc. Japan–U.S. Seminar on Two-Phase Flow Dynamics*, Kansai, Japan (1979).
17. A. Serizawa, I. Kataoka and I. Michiyoshi, Phase distribution in bubbly flow, *Second International Workshop on Two-Phase Flow Fundamentals*, Troy, NY (1987).
18. I. Kataoka and A. Serizawa, Interfacial area concentration in bubbly flow, *Nucl. Engng Design* **120,** 163–180 (1990).